Integrity of Laser-Based Feature Extraction and Data Association

Mathieu Joerger, Michael Jamoom, Matthew Spenko, and Boris Pervan
Illinois Institute of Technology
Chicago, Illinois, U.S.A.
joermat@iit.edu

***Abstract*—In this paper, a new integrity risk evaluation method is developed and tested for laser and radar-based navigation algorithms using feature extraction (FE) and data association (DA). This work is intended for safety-critical autonomous vehicle navigation. FE and DA are two pre-estimator measurement processing steps that aim at repeatedly and consistently identifying landmarks in the environment. A major risk for safety in FE and DA is caused by incorrect associations (mistaking one landmark for another). To assess this risk, a criterion is first introduced at FE: it establishes the minimum normalized separation between landmarks ensuring that they can be reliably, quantifiably distinguished. Then, an innovation-based DA process is designed, which provides the means to evaluate the probability of incorrect associations while considering all potential measurement permutations. These algorithms are analyzed and tested, showing the impact of incorrect associations on safety risk.**

Keywords—data association, SLAM, navigation safety, integrity, autonomous vehicle

I. INTRODUCTION

This paper describes the design, analysis and testing of a new integrity risk monitoring method for laser or radar-based localization using feature extraction (FE) and data association (DA). FE and DA are pre-estimator measurement processing functions. They are implemented in many laser and radar-based navigation applications [1-15]. The methods developed in this paper provide the means to *quantify risks* involved with FE and DA, which is not fully addressed in the literature. This will help ensure navigation safety in life-critical applications, including in autonomous passenger vehicle (APV) localization.

Google's approach to have APVs drive millions of miles with minimal human intervention is currently the most publicized effort to demonstrate APV safety. At this time, Google cars have autonomously travelled an impressive 1.5 million miles [16]. But, the National Highway Traffic Safety Administration (NHTSA) reports about 3000 billion miles travelled each year on U.S. highways, with 30,000 deaths caused by traffic accidents [17, 18]. A purely experimental, complete proof that APVs match the level of safety of human driving would take about 400 years at Google's current testing rate (of approximately 250,000 test miles per year). This is assuming that no fatalities occur during that time, that no major APV upgrade is performed, and that the testing environment is representative of all U.S. roads. Other methods must also be employed to ensure APV safety.

As a complement to testing, this paper leverages prior analytical work carried out in civilian aviation. The focus is on navigation system safety. In aviation navigation, safety is assessed in terms of integrity. This top-level quantifiable performance metric is sensor- and platform-independent, and can thus be used to set certifiable requirements on individual system components to achieve *and prove* an overall level of safety. Integrity is a measure of trust in sensor information: integrity risk is the probability of undetected sensor errors causing unacceptably large positioning uncertainty [19].

Several methods have been established to predict the integrity risk in Global Navigation Satellite Systems (GNSS)-based aviation applications, which are instrumental in ensuring the safety of pilots and crew [19-22]. Unfortunately, the same methods do not directly apply to APVs, because ground vehicles operate under sky-obstructed areas where GNSS signals can be altered or blocked by buildings and trees.

APVs require sensors in addition to GNSS, including laser scanners or radars, whose raw information must be pre-processed before it can be used for navigation [8, 23-24]. A first class of algorithms establishes correlations between successive scans to estimate sensor changes in 'pose' (i.e., position and orientation) [25-28]. These processes can become inaccurate or cumbersome for APVs moving over multiple time epochs. A second class of algorithms provides sensor localization by tracking recognizable, static features in the environment. This is typically done in two steps, as illustrated in Fig.1: FE and DA [2,5,7,8]. The resulting information can then be iteratively processed using sequential estimators (e.g., Extended Kalman filter or EKF), which is convenient in many practical applications [8,23,24].

The problems that FE and DA are addressing are the following. First, landmarks in the environment are unidentified, and their observations do not come with a 'name tag' like a GNSS satellite signal's Pseudo Random Noise (PRN) number, for example. Thus, FE aims at identifying the few most consistently identifiable, viewpoint-invariant landmarks in the raw sensor data.

978-1-5090-2042-3/16/$31.00 © 2016 IEEE

Second, laser and radar provide pose estimation by comparing current-time observations, noted $\hat{\mathbf{z}}_k$ in Fig. 1, to prior knowledge of the landmarks. This prior knowledge comes either from a landmark map ($\hat{\mathbf{m}}_i$) or from past-time estimation ($\mathbf{h}_{i,k}(\bar{\mathbf{x}}_k)$) in Simultaneous Localization and Mapping (SLAM) [23,24]. $\hat{\mathbf{m}}_i$ and $\mathbf{h}_{i,k}(\bar{\mathbf{x}}_k)$ assume an ordering of landmarks designated by subscript i (there are many possible orderings). DA aims at assigning landmark feature estimates ($\hat{\mathbf{z}}_k$) to the corresponding feature parameters in the estimation process, i.e., at finding the ordering of landmarks, i , that matches the ordering of landmarks in $\hat{\mathbf{z}}_k$ over successive observations [4]. Incorrect association is a well-known problem that can lead to catastrophic navigation errors [29]. Therefore, the extracted features must not only be identifiable over repeated observations, but must also be distinguishable from one landmark to another.

FE and DA can be challenging in the presence of sensor uncertainty; it is why many sophisticated algorithms have been devised [1-15]. But, how can we prove whether these FE and DA methods are safe for life-critical APV navigation applications, and under what circumstances?

These research questions are mostly unexplored. The most relevant publications are found in literature on target-tracking. For example, in [1], the innovation-based nearest-neighbor DA criterion is introduced, which serves as basis in many practical implementations. Reference [30] provides a detailed derivation of the probability of correct association given measurements. However, this Bayesian approach is not well suited for safety-critical applications due to the lack of risk prediction capability, and to the problem of bounding the prior probability of association (a similar issue is encountered in [31]). Another insightful approach is followed in [32]. However, it makes approximations that would not guarantee safe operation, and it presents exact solutions that could only be evaluated using computationally expensive numerical methods, not adequate for real-time navigation. Also, the risk of FE is not addressed.

In response, in this work, a new, computationally efficient integrity risk evaluation method is developed that ensures the safety of localization using FE and DA.

Section II of this paper describes the main assumptions, and introduces the measurement model used in the rest of the paper. Section III presents the new integrity risk evaluation method. A multiple-hypotheses approach is employed to assess the impact of incorrect associations. We derive an analytical expression of the integrity risk due to incorrect associations by designing landmark-separation and association-selection tests at the FE and DA steps, respectively.

At the FE step, a probabilistic landmark separation measure is defined, and quantified for each possible landmark permutation. A minimum separation criterion is derived based on an allocated integrity risk requirement to ensure that landmarks are distinguishable. In this work, feature parameters can include landmark position coordinates and orientation angles (in a local East-North-Up navigation frame), as well as landmark shape, size, color, reflectivity properties, etc.

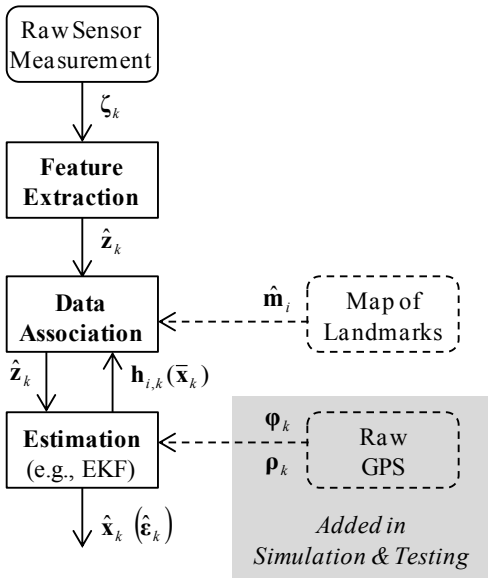

Fig. 1. Three Step Estimation Process for Laser or Radar-Based Navigation.

At the DA step, we employ a nearest neighbor association criterion [1], defined by the minimum normalized norm of the innovation vectors over all possible landmark permutations. We first use an illustrative example to establish the first known representation of the risk of incorrect association in innovation space. We then derive compact, analytical bounds on the probability of correct association, and on the integrity of navigation systems using DA and FE.

The integrity risk monitoring method is first evaluated by covariance analysis and direct simulation in Section IV, for landmark geometries representing an vehicle driving through a GNSS-denied environment. Simulation results demonstrate that the estimation error covariance is not an accurate measure of safety performance. In contrast, the integrity risk bound derived in this paper does account for potential incorrect associations.

Preliminary experimental testing is carried out in Section V. A set of data was collected in a structured environment using a multi-sensor system made of two two-dimensional laser scanners mounted back to back, and a carrier phase differential GPS implementation. The experiment shows that the proposed method can be used with actual sensor measurements to evaluate the integrity risk. Concluding notes are given in Section VI.

II. Overview of the Localization Process

This section provides an overview of the three step vehicle localization process outlined in Fig. 1. The section presents a measurement model and lists the main assumptions used throughout the paper.

A. Assumptions

This paper makes three main simplifying assumptions: (a) all landmarks are static; (b) sensor measurement equations can

be linearized; and (c) raw measurement errors can be over-bounded in the cumulative distribution function (CDF)-sense by Gaussian probability distributions [33,34].

Throughout the paper, subscript k designates a time-epoch. Let n_L be the total number of visible landmarks, and m_F the number of feature parameter estimated per landmark.

B. Extracted Feature Parameter Measurements

The raw laser or radar measurement equation at time k is written as:

$$\boldsymbol{\zeta}_k = \boldsymbol{\eta}_k(\mathbf{z}_k) + \boldsymbol{\omega}_k \tag{1}$$

where:

- $\boldsymbol{\zeta}_k$ is a vector of raw measurements, e.g., tens or hundreds of angular and ranging measurements for a laser scanner
- $\mathbf{z}_k$ is an $n\times 1$ vector of extracted feature parameters for all landmarks. The number of feature parameters is: $n \equiv n_L m_F$.

Vector $\boldsymbol{\omega}_k$ is normally distributed with zero mean and covariance matrix $\boldsymbol{\Omega}_k$. We use the notation:

$$\boldsymbol{\omega}_k \sim N(\mathbf{0}_{n\times 1},\ \boldsymbol{\Omega}_k) \tag{2}$$

where $\mathbf{0}_{a\times b}$ is an $a\times b$ matrix of zeros.

Let $\hat{\mathbf{z}}_k$ be an estimate of $\mathbf{z}_k$ derived from $\boldsymbol{\zeta}_k$, for example, using a weighted least squares estimator. We can write:

$$\hat{\mathbf{z}}_k \sim N\Big(\ \mathbf{z}_k\ ,\ \mathbf{V}_k \equiv (\boldsymbol{\Gamma}_k^T \boldsymbol{\Omega}_k^{-1} \boldsymbol{\Gamma}_k)^{-1}\Big) \tag{3}$$

where

$$\boldsymbol{\Gamma}_k \equiv \left.\frac{\partial \boldsymbol{\eta}_k}{\mathbf{z}}\right|_{\hat{\mathbf{z}}_k} \tag{4}$$

$\hat{\mathbf{z}}_k$ is the extracted feature parameter measurement vector.

C. Correctly-Associated Measurement Equation

For the correct association (indicated by the subscript 0), the extracted feature measurement equation can be written in terms of the system state parameter vector $\mathbf{x}_k$:

$$\hat{\mathbf{z}}_k = \mathbf{h}_{0,k}(\mathbf{x}_k) + \mathbf{v}_k \tag{5}$$

where

- $\mathbf{x}_k$ is the state vector, which includes vehicle pose parameters, and may also include constant landmark feature parameters when using a SLAM-type approach, as will be the case in Sections IV and V. Let m be the number of state parameters to be estimated. $\mathbf{x}_k$ is an $m\times 1$ vector.
- $\mathbf{v}_k$ captures the impact of raw measurement noise on $\hat{\mathbf{z}}_k$: $\mathbf{v}_k \sim N(\mathbf{0}_{n\times 1},\ \mathbf{V}_k)$, where $\mathbf{V}_k$ is defined in (3).

It is worth noting that, under the correct association hypothesis, the mean of $\hat{\mathbf{z}}_k$ is: $\mathbf{z}_k = \mathbf{h}_{0,k}(\mathbf{x}_k)$. Therefore, equation (3) becomes:

$$\hat{\mathbf{z}}_k \sim N\Big(\ \mathbf{h}_{0,k}(\mathbf{x}_k)\ ,\ \mathbf{V}_k\Big) \tag{6}$$

Equation (5) can be linearized about an estimate $\bar{\mathbf{x}}_k$ of $\mathbf{x}_k$:

$$\begin{aligned}\hat{\mathbf{z}}_k &= \mathbf{h}_{0,k}(\mathbf{x}_k) + \mathbf{h}_{0,k}(\bar{\mathbf{x}}_k) - \mathbf{h}_{0,k}(\bar{\mathbf{x}}_k) + \mathbf{v}_k \\ &\approx \mathbf{h}_{0,k}(\bar{\mathbf{x}}_k) + \mathbf{H}_k(\mathbf{x}_k - \bar{\mathbf{x}}_k) + \mathbf{v}_k\end{aligned} \tag{7}$$

where $\mathbf{H}_k \equiv \left.\dfrac{\partial \mathbf{h}_{0,k}}{\mathbf{x}}\right|_{\bar{\mathbf{x}}_k}$, $\mathbf{H}_k(\mathbf{x}_k - \bar{\mathbf{x}}_k) \approx \mathbf{h}_{0,k}(\mathbf{x}_k) - \mathbf{h}_{0,k}(\bar{\mathbf{x}}_k)$ (8)

Subscript 0 is not added to $\mathbf{H}_k$, which always assumes CA.

D. Vehicle State Estimation Under Correct Association

In addition, a linear model is assumed for the propagation of state parameters over time:

$$\mathbf{x}_k = \boldsymbol{\Phi}_{k-1}\mathbf{x}_{k-1} + \mathbf{w}_{k-1} \tag{9}$$

The following assumption is made for the process noise $\mathbf{w}_{k-1}$:

$$\mathbf{w}_{k-1} \sim N\big(\mathbf{0},\ \mathbf{W}_{k-1}\big) \tag{10}$$

For the system model described in (5) and (9), an EKF is used to estimate $\mathbf{x}_k$. The state prediction vector and prediction error covariance matrix are respectively given by:

$$\bar{\mathbf{x}}_k = \boldsymbol{\Phi}_{k-1}\hat{\mathbf{x}}_{k-1} \quad ,\quad \bar{\mathbf{P}}_k = \boldsymbol{\Phi}_{k-1}\hat{\mathbf{P}}_{k-1}\boldsymbol{\Phi}_{k-1}^T + \mathbf{W}_{k-1} \tag{11}$$

The state estimate vector and its error covariance matrix can be expressed as:

$$\hat{\mathbf{x}}_k = \bar{\mathbf{x}}_k + \mathbf{K}_k\boldsymbol{\gamma}_{0,k} \quad ,\quad \hat{\mathbf{P}}_k = \big(\mathbf{I} - \mathbf{K}_k\mathbf{H}_k\big)\bar{\mathbf{P}}_k \tag{11}$$

where

- $\boldsymbol{\gamma}_{0,k}$ is the $n\times 1$ innovation vector, under the correct association hypothesis (subscript 0):

$$\boldsymbol{\gamma}_{0,k} \equiv \hat{\mathbf{z}}_k - \mathbf{h}_{0,k}(\bar{\mathbf{x}}_k) \tag{12}$$

$\mathbf{K}_k$ is the Kalman gain:

$$\mathbf{K}_k = \bar{\mathbf{P}}_k \mathbf{H}_k^T \left(\mathbf{H}_k \bar{\mathbf{P}}_k \mathbf{H}_k^T + \mathbf{V}_k \right)^{-1} \tag{13}$$

In addition, the estimation error is defined as:

$$\hat{\boldsymbol{\varepsilon}}_k \equiv \hat{\mathbf{x}}_k - \mathbf{x}_k \tag{14}$$

Let us define the hazard state as the element, or linear combination of elements in $\mathbf{x}_k$, that is of primary concern for navigation safety. For example, for a vehicle driving in a lane on a highway, the positioning error in the direction perpendicular to the lane is of primary concern. The estimation error for the state of interest is given by:

$$\hat{\varepsilon}_k \equiv \boldsymbol{\alpha}^T \hat{\boldsymbol{\varepsilon}}_k \tag{15}$$

where

- $\boldsymbol{\alpha}$ is a vector of predefined coefficients, for example all zeros and a one for the East position coordinate when travelling on a North-South road.

Let σ_k^2 be the estimation error variance for the state of interest, under the correct association hypothesis: $\hat{\varepsilon}_k \sim N(0,\ \sigma_k^2)$. The challenge in this work is to evaluate the impact on $\hat{\varepsilon}_k$ of errors in FE and DA.

III. Integrity Risk Evaluation for Feature Extration and Data Association

This section presents the new multiple-hypothesis integrity risk evaluation method for FE and DA. The derivation starts in Section III.A with the definition of the DA fault model called incorrect association. The integrity risk is then defined in Section III.B, which outlines the quantities to be derived in the DA and FE steps, in Section III.C and III.D, respectively. The algorithm is summarized in Section III.E, where an analytical bound on the integrity risk accounting for the probability of correct association is given.

A. The Incorrect Association Problem and the Relevance of the Innovation Vector

The incorrect association (IA) differs from other fault modes in sensor-based navigation (such as, for example, GPS satellite clock faults causing ranging errors of all magnitudes) in that there is only a finite number of ways the DA process can fail. We can exploit this characteristic in a multiple hypothesis approach.

If n_L landmarks are extracted at time k, there are $(n_L!)$ potential landmark permutations, i.e., $(n_L!)$ ways to arrange the measurement equation (5), which we call $(n_L!)$ candidate associations. (For clarity of explanation, we assume that the total number of mapped landmarks, or of previously observed landmarks when using SLAM, is also the number n_L of extracted landmarks.)

IA occurs when the ordering of measurements in $\hat{\mathbf{z}}_k$ does not match the assumed ordering of landmarks in $\mathbf{h}_{i,k}(\bar{\mathbf{x}}_k)$. Subscript i designates association hypotheses, for $i = 0,\ldots,h$, where $h = n_L!-1$. We define $i = 0$ the fault-free, correct association (CA) hypothesis, the other h hypotheses are IA.

DA impacts the EKF estimation process in (11) through the innovation vector $\boldsymbol{\gamma}_{i,k}$ defined in (12) for the CA-case. $\boldsymbol{\gamma}_{i,k}$ is also an effective indicator of CA because it is zero mean only if the correct association was selected (recall that the mean of $\hat{\mathbf{z}}_k$ in equation (6) is $\mathbf{h}_{0,k}(\mathbf{x}_k)$).

In all IA cases, the mean of $\boldsymbol{\gamma}_{i,k}$ is not zero, which is expressed in terms of permutation matrices $\mathbf{A}_i$, for $i = 1,\ldots,\ h$, as:

$$\begin{aligned} \boldsymbol{\gamma}_{i,k} &= \hat{\mathbf{z}}_k - \mathbf{h}_{i,k}(\bar{\mathbf{x}}_k) \\ &= \mathbf{h}_{0,k}(\mathbf{x}_k) + \mathbf{v}_k - \mathbf{h}_{i,k}(\bar{\mathbf{x}}_k) + \mathbf{h}_{i,k}(\mathbf{x}_k) - \mathbf{h}_{i,k}(\mathbf{x}_k) \\ &= \mathbf{y}_{i,k} + \mathbf{v}_k - \mathbf{A}_{i,k}\mathbf{H}_k\bar{\boldsymbol{\varepsilon}}_k \end{aligned} \tag{16}$$

with

$$\mathbf{h}_{i,k} \equiv \mathbf{A}_{i,k}\mathbf{h}_{0,k} \tag{17}$$

$$\mathbf{y}_{i,k} \equiv \mathbf{B}_{i,k}\mathbf{h}_{0,k}(\mathbf{x}_k) \quad , \quad \mathbf{y}_{0,k} = \mathbf{0} \tag{18}$$

with

$$\mathbf{B}_{i,k} \equiv \mathbf{I}_n - \mathbf{A}_{i,k} \tag{19}$$

where $\mathbf{I}_a$ is the $a \times a$ identity matrix.

As an illustrative example, consider the case where IA hypothesis '$i = 1$' designates the event where landmark '1' is mistaken for landmark '2'. $\mathbf{A}_{i,k}$ and $\mathbf{B}_{i,k}$ take the following forms:

$$\mathbf{A}_{1,k} = \begin{bmatrix} \mathbf{0} & \mathbf{I} & \mathbf{0} \\ \mathbf{I} & \mathbf{0} & \mathbf{0} \\ \mathbf{0} & \mathbf{0} & \mathbf{I} \end{bmatrix} \quad , \quad \mathbf{B}_{1,k} = \begin{bmatrix} \mathbf{I} & -\mathbf{I} & \mathbf{0} \\ -\mathbf{I} & \mathbf{I} & \mathbf{0} \\ \mathbf{0} & \mathbf{0} & \mathbf{0} \end{bmatrix}$$

where $\mathbf{0}$ and $\mathbf{I}$ are matrices of appropriate sizes (subscripts were dropped for conciseness).

Equation (16) shows that an IA simultaneously affects multiple measurements, and that it causes a shift $\mathbf{y}_{i,k}$ in the mean of $\boldsymbol{\gamma}_{i,k}$, as well as a modification of the random errors from $\mathbf{H}_k\bar{\boldsymbol{\varepsilon}}_k$ for CA to $\mathbf{A}_i\mathbf{H}_k\bar{\boldsymbol{\varepsilon}}_k$ for IA.

B. Overall Integrity Risk Equation

The integrity risk $P(HMI_k)$, or probability of hazardous misleading information (HMI), is defined as the probability of the estimation error $\hat{\varepsilon}_k$ exceeding a predefined limit of acceptability, also called alert limit ℓ (as specified, for example, in [19] for aviation applications):

$$P(HMI_k) \equiv P\left(|\hat{\varepsilon}_k| > \ell\right) \tag{20}$$

Considering the mutually exclusive, exhaustive hypotheses of CA and IA, $P(HMI_k)$ can be expressed using the law of total probability as:

$$\begin{aligned} P(HMI_k) &= P(HMI_k, CA_K) + P(HMI_k, IA_K) \\ &= P(HMI_k \mid CA_K)P(CA_K) \\ &\quad + P(HMI_k \mid IA_K)[1 - P(CA_K)] \\ &\le 1 - [1 - P(HMI_k \mid CA_K)]P(CA_K) \end{aligned} \tag{21}$$

where

- CA_K is the correct association hypothesis for all landmarks at all times
- IA_K is the union of all IA hypotheses over all landmark combinations, at past and current times

We use the notation 'capital letter K' to designate a range of indices: $K \equiv \{0,\ldots,k\}$. In (21), $P(HMI_k \mid IA_K)$ was safely upper-bounded by $P(HMI_k \mid IA_K) = 1$ because the probability of an IA causing HMI is high, especially when IA can have occurred at any current or past time.

The remaining term $P(HMI_k \mid CA_K)$ in (21) is straightforward to evaluate: $P(HMI_k \mid CA_K)$ is given by:

$$\begin{aligned} P(HMI_k \mid CA_K) &= P\left(|\hat{\varepsilon}_k| < \ell \;\middle|\; CA_K\right) \\ &\le Q\left(\frac{\ell}{\sigma_k}\right) + 1 - Q\left(\frac{-\ell}{\sigma_k}\right) \end{aligned} \tag{22}$$

where $Q(\,)$ is the tail probability function of the standard normal distribution.

The variance σ_k^2 is often used to evaluate laser-based navigation system performance (e.g., in [8]). Equation (21) shows that σ_k^2 is an insufficient metric in safety-critical applications because $P(CA_K)$ must be accounted for. Evaluating $P(CA_K)$ is challenging, and is the main focus of most of this section.

First, the DA process is carried out over multiple epochs, all of which are included in the CA_K-event. Let us evaluate at each time j, for $j = 0,\ldots,k$, the probability of CA assuming that past associations were all correct: $P(CA_j \mid CA_{J-1})$. When using SLAM, we define $P(CA_0) \equiv 1$ because there is no association with previous observations at time zero. $P(CA_K)$ can then be iteratively evaluated, without having to make an assumption on the independence of events CA_j, as:

$$P(CA_K) = P(CA_0,\ CA_1,\ldots,\ CA_k) = \prod_{j=1}^{k} P(CA_j \mid CA_{J-1}) \tag{23}$$

Ultimately, the safety criterion is that $P(HMI_k)$ must meet a predefined integrity risk requirement I_{REQk}, which is set by a certification authority (similar to requirements set by the Federal Aviation Administration in [19]). The integrity risk requirement may be expressed as:

$$P(HMI_k) \le I_{REQk} \tag{24}$$

The expression of $P(HMI_k)$ in (21) will be refined to account for uncertainty in FE.

C. Association Candidate Validation

To lighten notations in Sections III-C and III-D, we drop the time subscript k. We also drop the conditional '$\mid CA_{K-1}$' in (23), with the understanding that probabilities of correct and incorrect associations at time k, $P(CA)$ and $P(IA)$, assume that all prior associations are correct.

1) Data Association Criterion: The nearest neighbor association criterion [1] is defined by the minimum norm of innovation vectors $\boldsymbol{\gamma}_i$, weighted by the inverse innovation covariance matrix $\mathbf{Y}_i^{-1}$, over all possible landmark permutations $i = 0,\ldots,h$. The association criterion is expressed as:

$$\min_{i=0,\ldots,h} \left\| \boldsymbol{\gamma}_i \right\|_{\mathbf{Y}_i^{-1}} \tag{25}$$

where $\left\| \boldsymbol{\gamma}_i \right\|_{\mathbf{Y}_i^{-1}} = \sqrt{\boldsymbol{\gamma}_i^T \mathbf{Y}_i^{-1} \boldsymbol{\gamma}_i}$, $\mathbf{Y}_i = \mathbf{A}_i \mathbf{H} \bar{\mathbf{P}} \mathbf{H}^T \mathbf{A}_i^T + \mathbf{V}$ (26)

2) Example Innovation Space Representation: To illustrate the criterion in (25), we use the one-dimensional example displayed in Fig. 2.

The problem in Fig. 2 is to estimate the position x of the sensor (upward pointing triangle) on a one-dimensional navigation reference axis $\boldsymbol{R}$, given the positions d_A, d_B and d_C of three landmarks on $\boldsymbol{R}$ (black circles), and using a set of noisy relative measurements z_1, z_2 and z_3 between sensor and landmarks. The challenge of DA is, in the presence of sensor errors, to find the ordering of landmarks $\{d_A,\ d_B,\ d_C\}$ corresponding the ordering of measurements $\{z_1,\ z_2,\ z_3\}$.

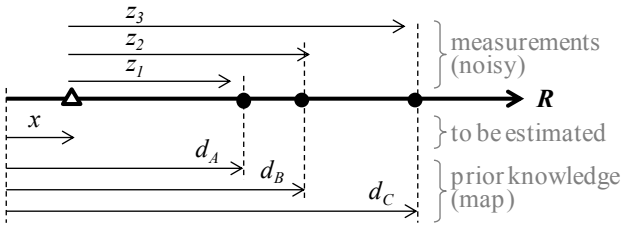

Fig. 2. Illustrative One-Dimensional Example

In this instance, the number of landmarks is $n_L = 3$, and the number of possible permutations is $(n_L!) = 6$, i.e., we consider six innovation vectors $\boldsymbol{\gamma}_i$. Vector $\boldsymbol{\gamma}_i$ is zero-mean only for the CA $i = 0$, which is why the association criterion in (25) selects the minimum norm $\|\boldsymbol{\gamma}_i\|_{\mathbf{Y}_i^{-1}}$.

The DA criterion is represented in innovation space in Fig. 3. In this example, the number of features per landmark is $m_F = 1$, and the innovation space is three-dimensional ($n = n_L m_F = 3$). The impact of DA on the mean normalized innovation vectors $\breve{\mathbf{y}}_i \equiv \mathbf{Y}_i^{-1/2}\mathbf{y}_i$ can be represented for all six landmark permutations, for $i = 0,\ldots,5$. Vectors $\breve{\mathbf{y}}_i$ lay in a space of dimension $n - m_F$, in this case, in a plane, and $\breve{\mathbf{y}}_0$ is at the origin.

In addition, in Fig. 3, 10,000 random samples of measurements z_1, z_2, z_3 were simulated. Equation (25) was used to distinguish correctly associated samples in blue, from incorrectly associated samples in red. The probability of correct association $P(CA)$, which we are trying to determine, is ratio of blue samples over the total number of samples. The next paragraphs provide an analytical expression for $P(CA)$.

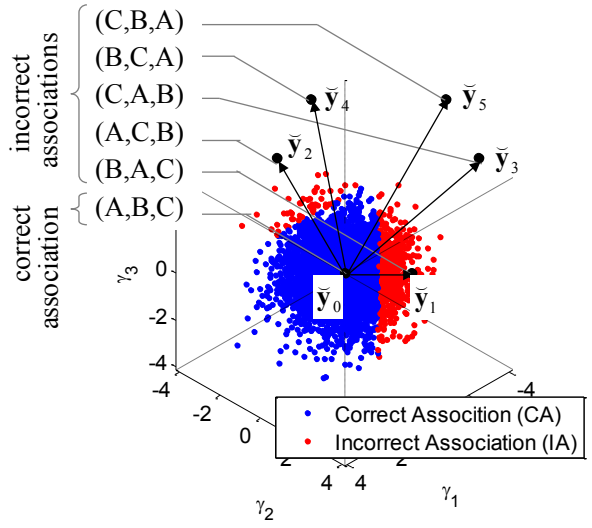

Fig. 3. Innovation-Space Representation

3) Probability of Correct Association: IA occurs if, for any i other than 0, the following inequality is verified:

$$\|\boldsymbol{\gamma}_i\|_{\mathbf{Y}_i^{-1}} \le \|\boldsymbol{\gamma}_0\|_{\mathbf{Y}_0^{-1}} \tag{27}$$

Anticipating the fact that the correlation between $\boldsymbol{\gamma}_i$ and $\boldsymbol{\gamma}_0$ has to be account for, (16) is rewritten as:

$$\boldsymbol{\gamma}_i = \mathbf{y}_i + \begin{bmatrix}\mathbf{I} & -\mathbf{A}_i\mathbf{H}\end{bmatrix}\begin{bmatrix}\mathbf{v}\\ \bar{\boldsymbol{\varepsilon}}\end{bmatrix} = \mathbf{y}_i + \mathbf{M}_i^T\mathbf{r} \tag{28}$$

where
$$\mathbf{M}_i \equiv \begin{bmatrix}\mathbf{I}\\ -\mathbf{A}_i\mathbf{H}\end{bmatrix}, \quad \mathbf{r} \equiv \begin{bmatrix}\mathbf{v}\\ \bar{\boldsymbol{\varepsilon}}\end{bmatrix} \tag{29}$$

$$\mathbf{r} \sim N\left(\mathbf{0},\ \mathbf{R} \equiv \begin{bmatrix}\mathbf{V} & \mathbf{0}\\ \mathbf{0} & \bar{\mathbf{P}}\end{bmatrix}\right) \tag{30}$$

Substituting (28) into (27), the following inequality can be written:

$$\|\mathbf{y}_i\|_{\mathbf{Y}_i^{-1}} - \|\mathbf{M}_i^T\mathbf{r}\|_{\mathbf{Y}_i^{-1}} \le \|\mathbf{M}_0^T\mathbf{r}\|_{\mathbf{Y}_0^{-1}} \tag{31}$$

because it is always true that:

$$\|\mathbf{y}_i\|_{\mathbf{Y}_i^{-1}} - \|\mathbf{M}_i^T\mathbf{r}\|_{\mathbf{Y}_i^{-1}} \le \|\mathbf{y}_i + \mathbf{M}_i^T\mathbf{r}\|_{\mathbf{Y}_i^{-1}} \tag{32}$$

Equation (31) is equivalent to

$$\|\mathbf{y}_i\|_{\mathbf{Y}_i^{-1}} \le \|\mathbf{M}_0^T\mathbf{r}\|_{\mathbf{Y}_0^{-1}} + \|\mathbf{M}_i^T\mathbf{r}\|_{\mathbf{Y}_i^{-1}} \tag{33}$$

Let us define the $(n+m)\times 1$ vector of independently, identically distributed random variables $\mathbf{q} \equiv \mathbf{R}^{-1/2}\mathbf{r}$. We have: $\mathbf{q} \sim N(\mathbf{0}_{(n+m)\times 1},\ \mathbf{I}_{n+m})$. Also, let $\lambda^2_{MAX,i}$ and $\lambda^2_{MAX,0}$ respectively be the maximum eigenvalues of $\mathbf{R}^{1/2}(\mathbf{M}_i\mathbf{Y}_i^{-1}\mathbf{M}_i^T)\mathbf{R}^{1/2}$ and $\mathbf{R}^{1/2}(\mathbf{M}_0\mathbf{Y}_0^{-1}\mathbf{M}_0^T)\mathbf{R}^{1/2}$. We use an upper-bound for the right hand side of (33):

$$\|\mathbf{y}_i\|_{\mathbf{Y}_i^{-1}} \le \sqrt{\mathbf{q}^T\mathbf{q}}\left(\lambda_{MAX,i} + \lambda_{MAX,0}\right) \tag{34}$$

The Appendix shows that $\lambda^2_{MAX,i} = 1$ and $\lambda^2_{MAX,0} = 1$, so that (34) is equivalent to:

$$q^2 \ge \frac{y_i^2}{4} \tag{35}$$

where $$q^2 \equiv \mathbf{q}^T\mathbf{q} \quad , \quad y_i^2 \equiv \left\|\mathbf{y}_i\right\|^2_{\mathbf{Y}_i^{-1}} \tag{36}$$

q^2 is chi-squared distributed with $n+m$ degrees of freedom (where $n+m$ is the number of measurements n plus the number of states m, i.e., the length of $\mathbf{v}$ plus length of $\bar{\boldsymbol{\varepsilon}}$).

It follows that the probability of correct association $P(CA)$ can be lower-bounded using the following inequality:

$$\begin{aligned} P(CA) &= 1 - P(IA) \\ &= 1 - P\left(\bigcup_{i=1}^{h}\left\|\boldsymbol{\gamma}_i\right\|^2_{\mathbf{Y}_i^{-1}} \le \left\|\boldsymbol{\gamma}_0\right\|^2_{\mathbf{Y}_0^{-1}}\right) \\ &\ge 1 - P\left(\bigcup_{i=1}^{h} q^2 \ge \frac{y_i^2}{4}\right) \\ &\ge 1 - P\left(q^2 \ge \min_{i=1,\ldots,h}\left(\frac{y_i^2}{4}\right)\right) \end{aligned} \tag{37}$$

Substituting (37) into (23) for $P(CA_j \mid CA_{J-1})$, and the result into (21), provides an upper-bound on the integrity risk $P(HMI_k)$.

Equation (37) is expressed in terms of the norm squared y_i^2 of the mean normalized innovation vectors $\breve{\mathbf{y}}_i$ represented in Fig. 3. However, in practice, we are given one sample of $\boldsymbol{\gamma}_i$, but we do not know the mean of its distribution. Fortunately, FE provides the means to establish a lower bound on y_i^2.

D. Extracted Feature Separation Criterion

Our approach to bound $P(HMI_k)$ leverages the FE step to ensure that features are distinguishable, hence easier to associate. The objective is to guarantee, with quantifiable integrity, that there is a minimum distance between landmarks.

At the FE step, all feature measurements are known, and are stacked in $\hat{\mathbf{z}}$. In addition, a comprehensive set of landmark permutations matrices can also be established, so that matrices $\mathbf{B}_i$, for $i = 1,\ldots,h$, are easily obtained. Given an IA hypothesis i, the following landmark 'separation' vector is defined:

$$\hat{\mathbf{d}}_i \equiv \mathbf{B}_i\hat{\mathbf{z}} = \mathbf{B}_i\left(\mathbf{h}_{0,k}(\mathbf{x}) + \mathbf{v}_k\right) \tag{38}$$

$$\hat{\mathbf{d}}_i \sim N\left(\ \mathbf{y}_i\ ,\ \mathbf{D}_i \equiv \mathbf{B}_i\mathbf{V}\mathbf{B}_i^T\right) \tag{39}$$

The mean of $\hat{\mathbf{d}}_i$ is $\mathbf{y}_i$ (defined in (18)), whose norm we are trying to evaluate.

It is worth noting that $\mathbf{B}_i$ is rank deficient, with rank values ranging from m_F to $n - m_F$ depending on how many landmarks are involved in permutation i, for $i = 1,\ldots,h$. Let r_i be the rank of $\mathbf{B}_i$. An orthogonal decomposition of the symmetric positive semi definite matrix $\mathbf{D}_i$ is expressed as:

$$\mathbf{D}_i = \begin{bmatrix}\mathbf{U}_i & \mathbf{U}_{i,0}\end{bmatrix}\begin{bmatrix}\mathbf{S}_i & \mathbf{0} \\ \mathbf{0} & \mathbf{0}\end{bmatrix}\begin{bmatrix}\mathbf{U}_i^T \\ \mathbf{U}_{i,0}^T\end{bmatrix} = \mathbf{U}_i\mathbf{S}_i\mathbf{U}_i^T \tag{40}$$

where $\mathbf{S}_i$ is a diagonal matrix of non-zero singular values, and $\mathbf{U}_i$ is an orthogonal matrix: $\mathbf{U}_i^T\mathbf{U}_i = \mathbf{U}_i\mathbf{U}_i^T = \mathbf{I}_{r_i}$.

For each potential IA, we define the normalized separation metric as:

$$\hat{d}_i^2 \equiv \hat{\mathbf{d}}_i^T\mathbf{U}_i\mathbf{S}_i^{-1}\mathbf{U}_i^T\hat{\mathbf{d}}_i \tag{41}$$

$\hat{d}_i^2$ can be expressed as the norm squared of the $r_i \times 1$ vector $\mathbf{S}_i^{-1/2}\mathbf{U}_i^T\hat{\mathbf{d}}_i$, which follows $N(\mathbf{S}_i^{-1/2}\mathbf{U}_i^T\mathbf{y}_i\ ,\ \mathbf{I}_{r_i})$. Therefore, $\hat{d}_i^2$ is non-centrally chi-square distributed with r_i degrees of freedom and with non-centrality parameter noted d_i^2. We use the notation:

$$\hat{d}_i^2 \sim \chi^2\left(r_i\ ,\ d_i^2 \equiv \mathbf{y}_i^T\mathbf{U}_i\mathbf{S}_i^{-1}\mathbf{U}_i^T\mathbf{y}_i\right) \tag{42}$$

Let T_i^2 be a FE threshold that ensures a desired separation between extracted landmarks given the sensor range, sensor errors, and if available, based on prior knowledge of the environment. In future work, T_i^2 will be set to meet a predefined continuity risk requirement allocation, as further explained in Section IV. For now, in this paper, it is heuristically set offline, by trial and error. Landmarks are extracted if and only if:

$$\hat{d}_i^2 \ge T_i^2 \tag{43}$$

The separation measure $\hat{d}_i^2$ is affected by sensor errors. The following derivation establishes with quantifiable confidence, the minimum value L_i^2 of the mean separation d_i^2. L_i^2 is defined as:

$$P(d_i^2 \le L_i^2 \mid \hat{d}_i^2 \ge T_i^2) < I_{FE,REQ,i} \tag{44}$$

where $I_{FE,REQ,i}$ is a sub-allocation of $I_{FE,REQ}$, which is itself a small portion of the overall integrity risk requirement I_{REQ}. $I_{FE,REQ}$ is divided among h IA hypotheses as:

$$\sum_{i=1}^{h} I_{FE,REQ,i} = I_{FE,REQ} \quad \text{e.g.,} \quad I_{FE,REQ,i} = I_{FE,REQ}/h \tag{45}$$

$I_{FE,REQ}$ must be added to $P(HMI_k)$ in (21). Given that $P(\hat{d}_i^2 \geq T_i^2) = 1$ as captured in (43), (44) can be rewritten using Bayes' theorem as:

$$\begin{aligned} P(d_i^2 \leq L_i^2 \mid \hat{d}_i^2 \geq T_i^2) &\leq P(\hat{d}_i^2 \geq T_i^2 \mid d_i^2 = L_i^2) \\ &\leq P(\hat{\varepsilon}_{D,i}^2 \geq T_i^2 - L_i^2) \end{aligned} \tag{46}$$

where $$\hat{\varepsilon}_{D,i}^2 \equiv \hat{d}_i^2 - d_i^2 \quad , \quad \hat{\varepsilon}_{D,i}^2 \sim \chi^2(r_i, 0) \tag{47}$$

Fig. 4 provides an illustration of the variables in (46) for a hypothetical one-degree-of-freedom $\hat{d}_i$ -example, whose probability density function (PDF) can be represented as a Gaussian function. We want to find the mean value L_i such that the probability of $\hat{d}_i$ exceeding T_i is lower than $I_{FE,REQ,i}$. It follows that L_i^2, for $i = 1, \ldots, h$, is determined as:

$$\int_{T_i^2 - L_i^2}^{+\infty} \chi^2(r_i, 0) = I_{FE,REQ,i} \tag{48}$$

L_i^2 is the minimum value of the mean separation vector norm squared d_i^2 that can be ensured with probability larger than $1 - I_{FE,REQ,i}$. In mathematical terms, the following bound is ensured with pre-allocated integrity:

$$d_i^2 = \mathbf{y}_i^T \mathbf{U}_i \mathbf{S}_i^{-1} \mathbf{U}_i^T \mathbf{y}_i \geq L_i^2 \tag{49}$$

This result can be used in (37) to address the fact that y_i^2 is unknown. y_i^2, which is defined in (36), is rewritten by pre- and post-multiplying the weighting matrix $\mathbf{Y}_i^{-1}$ by the identity matrix $(\mathbf{U}_i \mathbf{S}_i^{-1/2} \mathbf{U}_i^T)(\mathbf{U}_i \mathbf{S}_i^{1/2} \mathbf{U}_i^T)$:

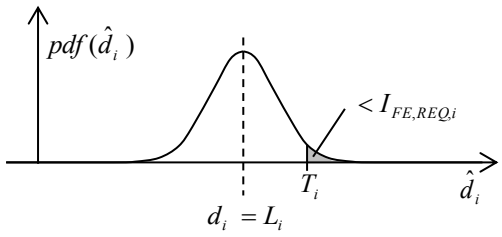

Fig. 4. One-Degree-of-Freedom Representation for the Derivation of L_i

$$y_i^2 = \mathbf{y}_i^T \mathbf{U}_i \mathbf{S}_i^{-1/2} \mathbf{U}_i^T (\mathbf{U}_i \mathbf{S}_i^{1/2} \mathbf{U}_i^T \mathbf{Y}_i^{-1} \mathbf{U}_i \mathbf{S}_i^{1/2} \mathbf{U}_i^T) \mathbf{U}_i \mathbf{S}_i^{-1/2} \mathbf{U}_i^T \mathbf{y}_i \tag{50}$$

y_i^2 can be lower-bounded using the following inequality:

$$y_i^2 \geq \mathbf{y}_i^T \mathbf{U}_i \mathbf{S}_i^{-1} \mathbf{U}_i^T \mathbf{y}_i \lambda_{MIN,i}^2 \tag{51}$$

where $\lambda_{MIN,i}^2$ is the minimum eigenvalue of $(\mathbf{U}_i \mathbf{S}_i^{1/2} \mathbf{U}_i^T \mathbf{Y}_i^{-1} \mathbf{U}_i \mathbf{S}_i^{1/2} \mathbf{U}_i^T)$. The weighted norm squared of $\mathbf{y}_i$ appearing in (51) is d_i^2. Thus, y_i^2 can be further lower-bounded using (49) by:

$$y_i^2 \geq L_i^2 \lambda_{MIN,i}^2 \tag{52}$$

Finally, (52) is used to establish a bound on $P(CA)$ in (37), which is now expressed in terms of known quantities as:

$$P(CA) \geq 1 - P\left(q^2 \geq \min_{i=1,\ldots,h} \left(\frac{L_i^2 \lambda_{MIN,i}^2}{4} \right) \right) \tag{53}$$

E. Summary: Analytical Bound on Integrity Risk Accounting for Probability of Correct Association

In this section, we have established an analytical bound on the integrity risk that accounts for the risk of incorrect association. The integrity risk is expressed as:

$$\begin{aligned} &P(HMI_k) \\ &\leq 1 - \left[1 - P(HMI_k \mid CA_K)\right] \prod_{j=1}^{k} P(CA_j \mid CA_{J-1}) + I_{FE,REQ,k} \end{aligned} \tag{54}$$

with $$P(HMI_k \mid CA_K) = Q(\ell/\sigma_k) + 1 - Q(-\ell/\sigma_k) \tag{55}$$

$$P(CA_j \mid CA_{J-1}) \geq 1 - P\left(q_j^2 \geq \min_{i=1,\ldots,h} \{L_{i,j}^2 \lambda_{MIN,i,j}^2 / 4\} \right) \tag{56}$$

where

- k is an index identifying a time step
- $Q(\,)$ is the tail probability function of the standard normal distribution
- ℓ is the specified alert limit that defines a hazardous situation
- σ_k is the standard deviation of the estimation error for the vehicle state of interest
- $I_{FE,REQ,k}$ is a predefined integrity risk allocation at FE, chosen to be a small fraction of the over integrity risk requirement $I_{REQ,k}$.

q_j^2 is a chi-square distributed random variable with a number of degrees of freedom that is the sum of the number of measurements and of states at time step j

$L_{i,j}^2$ is defined at FE in (48), and represents the minimum value of the mean separation vector norm squared that is measured at FE at time step j.

$\lambda_{MIN,i,j}^2$ can be determined at DA, and is defined in (51) to account for the worst-case projection of the FE's separation vector into the DA's innovation space.

The analytical integrity risk bound in (54) to (56) is implemented, analyzed, and tested in the next two sections.

IV. Covariance Analysis and Direct Simulations

In this section, two example simulations first analyzed in [29,35] are modified to evaluate (54) to (56). The first scenario is an illustrative two-dimensional, two-landmark problem. Covariance can be analyzed assuming flawless FE and DA. However, the integrity risk bound in (54) to (56) will show cases where the covariance does not capture aspects of safety risk due to incorrect associations (IA).

A second scenario is simulated in a more realistic scenario, using a multi-sensor laser/GPS system onboard a vehicle roving across a GPS-denied area, and navigating using static landmarks. This direct simulation scenario helps quantify the significant impact of IA on $P(HMI_k)$, and is used to outline the next steps of this research, i.e., the need for a continuity risk evaluation method.

A. Illustrative Two Landmark Scenario

Fig. 5 and Fig. 7 represent a vehicle designated by an upward pointing triangle roving between two landmarks represented by black-shaded circles. The vehicle starts at an initial, known position at point (0, 0) in a local East-North reference frame, and uses measurements from a laser or radar to estimate its position. In this example, vehicle orientation is known (as if given by another sensor, e.g., a perfect inertial navigation system). While roving along the North axis, the vehicle passes by two point-feature landmarks. The actual landmark locations are initially unknown to the navigation system. Landmark locations are simultaneously estimated with vehicle pose in a SLAM-like approach. Simulation parameters are listed in Table 1.

Positioning errors at consecutive sample updates are represented by covariance ellipses in Fig. 5 and Fig. 7, for the locations of the vehicle (red ellipses) and landmarks (blue ellipses). These ellipses assume consistently successful FE and DA. We focus on the East-West positioning error, perpendicular to vehicle's straight line trajectory. Cross-track errors are of primary concern for navigation safety, and the cross-track direction is where errors are the largest. A cross-track drift over distance travelled is observed, which is typical of SLAM [14, 36, 37].

1) Case of Two Distinguishable Landmarks: In a first case, the actual landmark locations are at (-5, 15) and (5, 15). This relatively large separation makes them easy to distinguish, as suggested by the fact that the blue covariance ellipses for the left and right landmarks do not overlap.

Fig. 6 shows the integrity risk bound labeled $P(HMI_k)$, represented with a red curve, versus northward travel distance as the vehicles passes by the two landmarks. The bound is always larger than $I_{FE,REQ,k} = 10^{-8}$, which corresponds to our choice of an example integrity risk requirement allocation. As captured in (54), this $P(HMI_k)$ -bound is loose when $P(CA_K) \approx 1$ and $P(HMI_k \mid CA_K) \ll 10^{-8}$, which is the case in Fig. 6 for travel distances smaller than 30 m. The $P(HMI_k)$-bound captures the risk involved in FE, and is a practical bound when trying to achieve an overall example requirement of $I_{REQ,k} = 10^{-7}$.

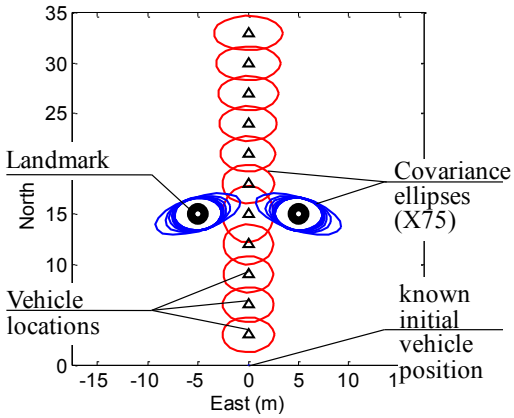

Fig. 5. Covariance Analysis for the Illustrative Two Distinguishable Landmark Scenario

TABLE I. Simulation Parameters

System Parameters	Values
Standard deviation on raw ranging measurement in (2)	0.02 m
Standard deviation on raw angular measurement in (2)	0.5 deg
Laser range Limit	20 m
Laser data sampling interval	0.5 s
Vehicle speed	1 m/s
Alert limit ℓ	0.5 m
Integrity risk allocation for FE, $I_{FE,REQ,k}$	10^{-8}

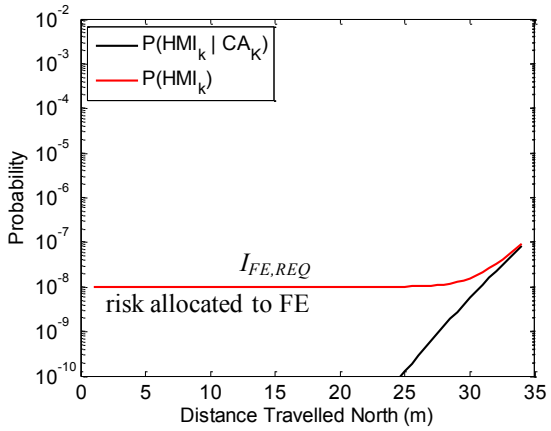

Fig. 6. Integrity Risk Bound for the Illustrative Two Distinguishable Landmark Scenario

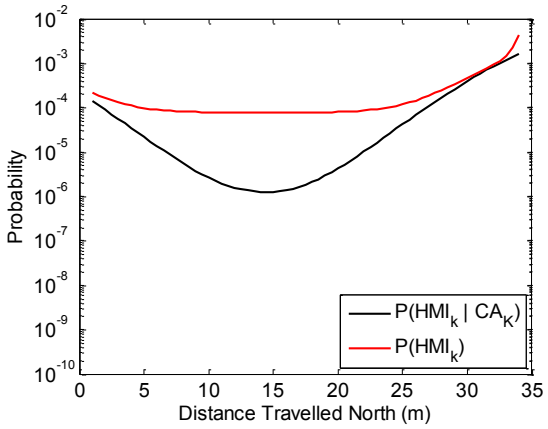

Fig. 8. Integrity Risk Bound for the Illustrative Two Difficult-to-Distinguish Landmark Scenario

In parallel, the black curve in Fig. 6 represents the bound on $P(HMI_k \mid CA_K)$, which is fully determined by the alert limit ℓ and the vehicle positioning covariance. This curve represents a vehicle navigation performance metric often used to evaluate laser-based navigation systems [14, 36, 37]. The black curve converges with our integrity risk bound (red curve) for travel distances larger than 30 m. In this example, the black curve adequately captured the safety risk, because $P(CA_K) \approx 1$. But, the next section will show that it is not always the case.

2) Case of Two Difficult-to-Distinguish Landmarks: In this second case, the two landmark locations represented in Fig. 7 are at (-2, 15) and (2, 15), which makes them difficult to distinguish. The blue covariance ellipses for the two landmarks do overlap with each other.

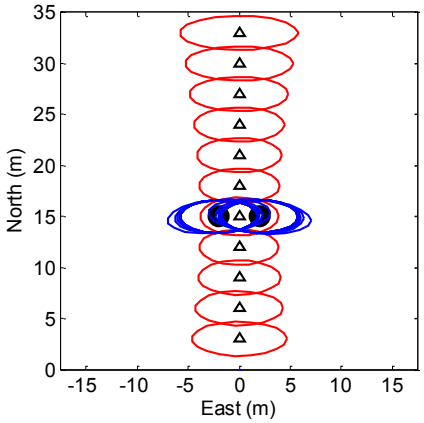

Fig. 7. Covariance Analysis for the Illustrative Two Difficult-to-Distinguish Landmark Scenario

Fig. 8 displays the $P(HMI_k)$-bound in red, and the $P(HMI_k \mid CA_K)$-bound in black, versus travel distance. Both curves are orders of magnitude higher than in Fig. 6. This is because the change in geometry between vehicle and landmarks provides less information on vehicle cross-track deviation in Fig. 7 than it did in Fig. 5. (The estimation process is detailed in [35].) This can also be seen with the red ellipses, which are horizontally more elongated in Fig. 7 as compared to Fig. 5.

The $P(HMI_k)$-bound shows the impact of possible incorrect associations on the integrity risk. It can be noted that there is a substantial difference between the red and black curves, especially for a travel distance of 15 m where the vehicle is right between landmarks. In this case, the covariance-based $P(HMI_k \mid CA_K)$-bound is two orders of magnitude below the $P(HMI_k)$-bound. From a safety perspective, the covariance is a misleading navigation performance metric.

B. Vehicle Roving Through a GPS-Denied Area

This analysis investigates the safety performance of a multi-sensor GPS/laser system embedded on a vehicle roving through a forest. GPS signals are blocked by the tree canopy, and low-elevation satellite signals do not penetrate under the trees. Tree trunks are used as landmarks by the laser-based SLAM-type algorithm.

The measurement vector $\hat{\mathbf{z}}_k$ in (5) is augmented with GPS code and carrier measurements, and the state vector $\mathbf{x}_k$ is augmented to include an unknown GPS receiver clock bias and initially known carrier phase cycle ambiguities. Time-correlated GPS signals and non-linear laser data are processed in a unified time-differencing extended Kalman filter derived in [29, 35]. The simulation parameter values are listed in Table 1, and a standard differential GPS measurement error model is

used, which is described in [35]. In this scenario, GPS and lasers essentially relay each other with seamless transitions from open-sky through GPS-denied areas where landmarks modeled as poles with non-zero radii are visible.

Fig. 9 illustrates the interactions between the two sensors while the GPS/laser-equipped vehicle roves through the GPS-denied area. Three successive snap-shots (a, b, and c) of a direct simulation are presented. On the upper part, azimuth-elevation plots and simulated laser scans present respectively the GPS satellite sky blockage within the obstruction, and the landmarks within range of the laser. The simulated laser measurement error model includes both random uncertainty and large-size impulse-type ranging errors. The result of the estimation process is given on the lower part. Covariance ellipses represent the positioning error on the vehicle and landmarks.

The mission starts with the vehicle operating in a GPS available area (yellow-shaded). The many satellite signals available during this initialization enable accurate estimation of cycle ambiguities, so that the vehicle positioning uncertainty does not exceed a few centimeters. In the next time-steps, as the vehicle crosses the GPS-and-laser available area (green-shaded), and the laser-only area (blue-shaded), seamless variations in covariance are achieved. The yellow-green-blue color code is used consistently in the next figures. A detailed description of this simulation is given in [35].

In this scenario, the likelihood of incorrect association is high. This can be seen on the upper plot in Fig. 10. Fig. 10 shows the actual cross-track positioning error versus distance travelled significantly exceeding the corresponding one-sigma covariance envelope. It indicates that sources of error impact positioning, which are not captured by the covariance.

This is confirmed on the lower chart of Fig. 10, where the black curve showing the $P(HMI_k \mid CA_K)$-bound and directly derived from the positioning error covariance stays below 10^{-5}. In contrast, the red curve showing the $P(HMI_k)$-bound indicates much higher risk. The red curve reaches a first plateau of $I_{FE,REQ,k}$ due to the risk involved in FE when two landmarks are visible. As discussed in Section IV-A-1), our choice of $I_{FE,REQ,k} = 10^{-8}$ is conservative, but it is far below the overall requirement (e.g., assumed to be $I_{REQ,k} = 10^{-7}$) and provides a practical solution to $P(HMI_k)$-bounding when using FE.

The red $P(HMI_k)$-bound curve then suddenly increases to 1, at approximately 21 m of distance travelled. This means that there is not enough information to guarantee that any of the candidate associations is correct.

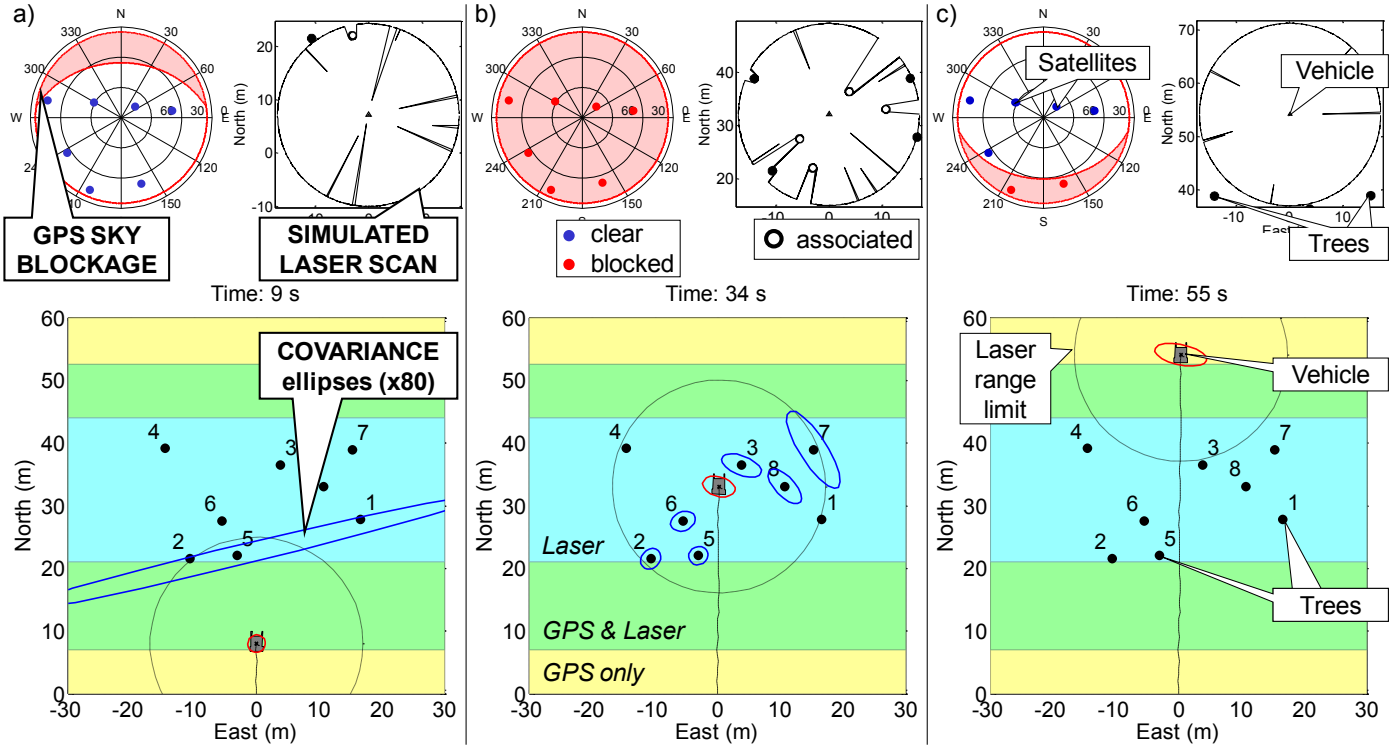

Fig. 9. Direct Simulation of the GPS/Laser Algorithm in the GPS-Denied Area Scenario: (a) the vehicle started in the GPS-available area (yellow-shaded) and enters the transitional GPS-and-laser-available area (green) where absolute landmark position is being estimated; (b) the vehicle is in the middle of the GPS obstruction are relies on laser/radar-only (blue-shaded area), so that the vehicle pose estimation error increases with travel distance; (c) the vehicle is back into a GPS available area (yellow), and the cross-track positioning drift is stopped.

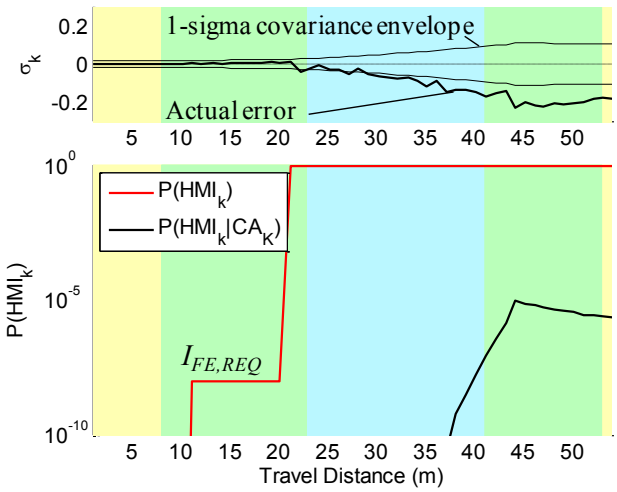

Fig. 10. $P(HMI_k)$-Bound for the GPS-Denied-Area Crossing Scenario (same color-code as in Fig. 9)

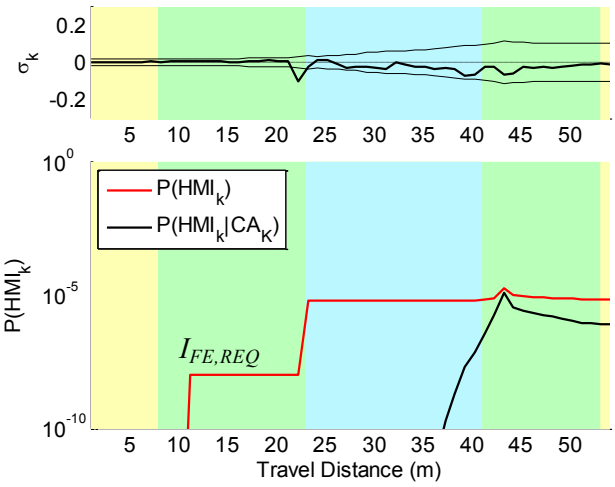

Fig. 12. $P(HMI_k)$-Bound for the GPS-Denied-Area Crossing Scenario when Landmark 6 is not Extracted(same color-code as in Fig. 9).

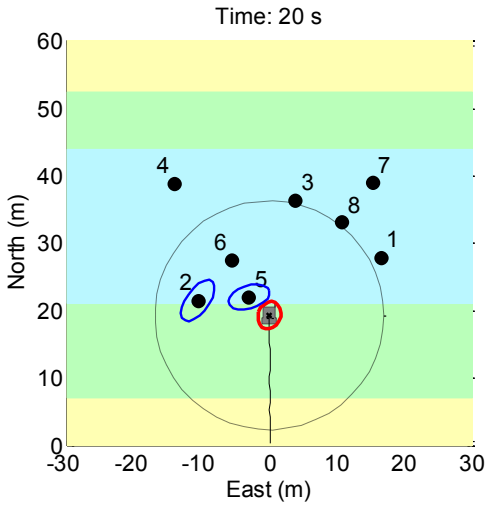

Fig. 11. Time-Step Preceding the Large Increase in $P(HMI_k)$-Bound in Fig. 10 (same color-code as in Fig. 9).

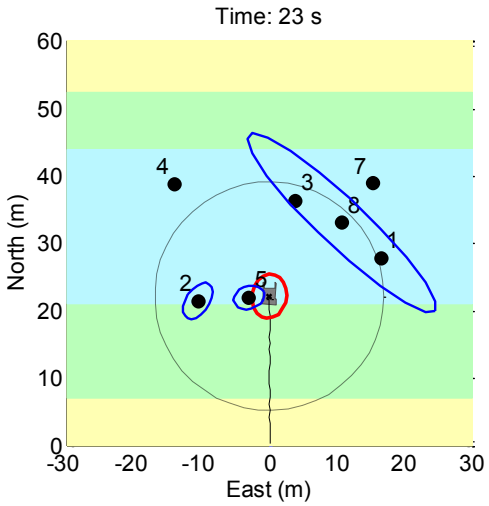

Fig. 13. Time-Step Preceding the Increase in $P(HMI_k)$-Bound in Fig. 12 when Landmark 6 is not Extracted (same color-code as in Fig. 9).

Fig. 11 shows that, at the time step preceding the large increase in predicted integrity risk, landmark 6 is hidden behind landmark 5. Before that point, it was either out of laser range, or hidden behind landmark 5. It will first become visible to the laser at the next time step, which makes correct measurement association with either landmark 5 or 6 extremely challenging. The $P(HMI_k)$-bound in (54) to (56) provides the means to quantify the impact on integrity risk of such events.

Moreover, the method proposed in Section III allows to avoid such cases by increasing the FE threshold T_i^2 in (43), so that landmark 6 would not be extracted.

Not extracting landmark 6 reduces occurrences of incorrect associations, as indicated in the upper graph of Fig. 12 where the positioning error now fits the covariance envelope. Risk reduction is also observed in the lower chart, where the $P(HMI_k)$-bound does not exceed 10^{-5} (versus 1 in Fig. 10). The red curve in Fig. 12 still exhibits a sudden increase at about 23 m of travel distance. This is because, as shown in Fig. 13, landmark 2 which was temporarily hidden behind landmark 5 will suddenly become visible again. The resulting risk of incorrectly associating measurements with landmarks 2 or 5 is quantified as being about 10^{-5}.

This risk can be further reduced by increasing the FE threshold T_i^2 again. But, first, this approach is heuristic, and

tuning T_i^2 in real time is not a practical solution. Second, if T_i^2 is further increased, it will become large enough that there will not be enough extracted measurements to provide *continuous* positioning. Thus, we want to set T_i^2 to meet a predefined continuity risk requirement, as specified for example in aviation applications [19].

This section has pointed out a key tradeoff in laser-based navigation safety: on the one hand, a large number of extracted measurements ensures continuous positioning, but on the other hand, it lowers navigation integrity because it increases the risk of incorrect associations. Future work will investigate ways to quantify continuity risk, and will explore this tradeoff.

V. Preliminary Experimental Testing

Preliminary experimental testing of the method in Section III is carried out using data collected in a structured environment shown in Fig. 14. Static simple-shaped landmarks are located at locations sparse enough to ensure successful outcomes for FE and DA. Because the results presented here are free of incorrect associations, they describe the estimation process, and $P(HMI_k)$ is expected to match $P(HMI_k \mid CA_K)$.

Measurements from carrier phase differential GPS (CPDGPS) as well as laser scanners are synchronized and recorded. In order to obtain a full 360 deg laser scan, two 180deg laser scanners are assembled back-to-back. The laser scanners have a specified 15-80 m range limit, a 0.5 deg angular resolution, a 5 Hz update rate and a ranging accuracy of 1-5 cm (1 sigma) [38]. The GPS antenna is mounted on top of the front laser. The lever-arm distance between the two lasers is included in the measurement model.

The two lasers and the GPS antenna are mounted on rover also carrying the GPS receiver and data-link. An embedded computer onboard the vehicle records all measurements including the raw GPS data from the reference station transmitted via wireless spread-spectrum data-link. Truth vehicle trajectory and landmark locations are obtained using a fixed CPDGPS solution.

In this forest-type scenario, landmarks are tree-trunks reproduced using five cardboard columns and one dark plastic garbage can. Because there is actually no physical obstruction to the sky, satellite masking for the GPS/laser integration system is performed artificially as illustrated in Fig. 14: an artificially simulated tree canopy blocks high-elevation satellite signals; low-elevation GPS observations are not used either inside the obstruction.

As mentioned in the first paragraph of this section, the landmark geometry in this experiment is such that the risk of incorrect association is extremely small. This is confirmed on the upper chart in Fig. 15 where the actual error (thick line) fits the covariance envelope (thin line) throughout the test. The lower graph also shows that the $P(HMI_k)$-bound matches the $P(HMI_k \mid CA_K)$-bound, except between 565 m and 600 m of travel distance where the predefined integrity risk allocation for FE is the dominant term in the $P(HMI_k)$-bound.

This test demonstrates that the method derived in this paper can be implemented using actual data from a multi-sensor GPS/laser system, and that the analytical integrity risk bound is tight when the risk of incorrect association is small.

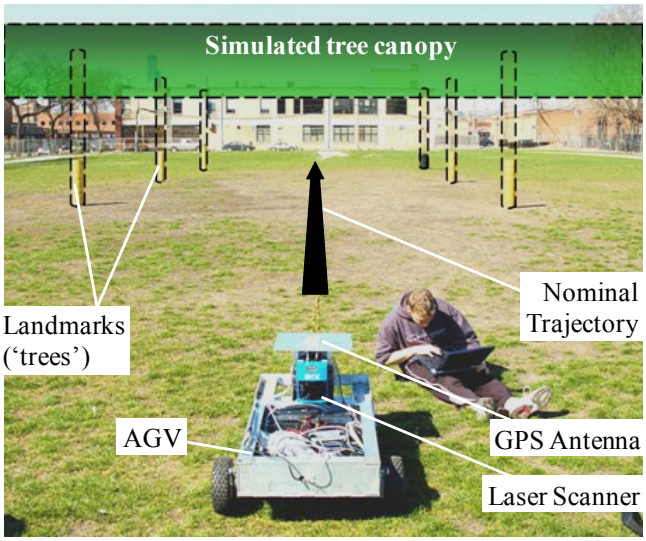

Fig. 14. Experimental Setup of a Forest-Type Scenario, where a GPS/Laser-Equipped Rover is driving by Six Landmarks (Cardboard Columns) in a GPS-Denied Area. GPS is Artificially Blocked by a Simulated Tree Canopy, and a Precise Differential GPS Solution is used as Truth Trajectory.

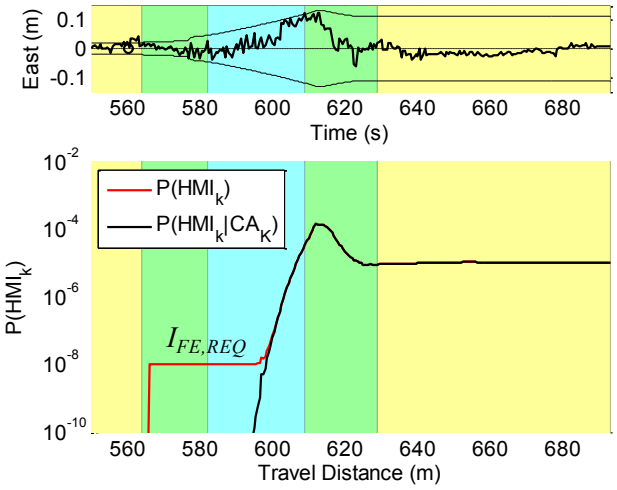

Fig. 15. Integrity Risk Bounds Versus Travel Distance for the Preliminary Experimental Data Set Capturing a Forest-Type Scenario (same color-code as in Fig. 9).

VI. CONCLUSION

This paper presents a new approach to ensure the safety of laser or radar-based navigation using feature extraction (FE) and data association (DA) by quantifying the integrity risk.

An analytical integrity risk bound is established, which accounts for all possible ways FE and DA can fail. First, at FE, a minimum normalized separation metric is derived, which guarantees, in a statistically quantifiable manner, that landmarks are distinguishable. Then, at DA, an innovation-based nearest-neighbor association criterion is employed to evaluate the risk of all potential incorrect associations, at each time step in the iterative vehicle pose estimation process.

Performance evaluations are carried out by covariance analysis and direct simulation, showing that the positioning error covariance is a misleading safety performance metric. Cases are shown where the contributions of incorrect associations to integrity risk far surpass that of nominal errors accounted for in the positioning error covariance. In addition, a key tradeoff in FE and DA is pointed out: more extracted measurements ensure *continuous* positioning, but reduce integrity because of the increased risk of incorrect association. The next step of this research will aim at quantifying the continuity risk of FE and DA, which is an essential aspect of navigation safety.

Finally, preliminary experimental testing was carried out using a multi-sensor GPS/laser system onboard a vehicle roving in a structured environment. It showed that the integrity risk evaluation method can be implemented with real data. Future testing will be performed in a more realistic passenger vehicle operating environment.

APPENDIX

This Appendix shows that: $\lambda_{MAX,i}=1$ and $\lambda_{MAX,0}=1$, where $\lambda^2_{MAX,i}$ and $\lambda^2_{MAX,0}$ respectively are the maximum eigenvalues of $\mathbf{R}^{1/2}(\mathbf{M}_i\mathbf{Y}_i^{-1}\mathbf{M}_i^T)\mathbf{R}^{1/2}$ and $\mathbf{R}^{1/2}(\mathbf{M}_0\mathbf{Y}_0^{-1}\mathbf{M}_0^T)\mathbf{R}^{1/2}$.

The following derivation shows that $\mathbf{R}^{1/2}(\mathbf{M}_i\mathbf{Y}_i^{-1}\mathbf{M}_i^T)\mathbf{R}^{1/2}$, which is symmetric (obvious), is also idempotent for $i=0,\ldots,h$. By definitions of $\mathbf{M}_i$ and $\mathbf{R}$ in (29) and (30), the following equations can be written:

$$
\begin{aligned}
&\mathbf{R}^{1/2}(\mathbf{M}_i\mathbf{Y}_i^{-1}\mathbf{M}_i^T)\mathbf{R}^{1/2}\mathbf{R}^{1/2}(\mathbf{M}_i\mathbf{Y}_i^{-1}\mathbf{M}_i^T)\mathbf{R}^{1/2}\\
&\quad=\mathbf{R}^{1/2}\mathbf{M}_i\mathbf{Y}_i^{-1}\begin{bmatrix}\mathbf{I} & -\mathbf{A}_i\mathbf{H}\end{bmatrix}\begin{bmatrix}\mathbf{V} & \mathbf{0}\\ \mathbf{0} & \overline{\mathbf{P}}\end{bmatrix}\begin{bmatrix}\mathbf{I}\\ -\mathbf{H}_i^T\mathbf{A}_i^T\end{bmatrix}\mathbf{Y}_i^{-1}\mathbf{M}_i^T\mathbf{R}^{1/2}\\
&\quad=\mathbf{R}^{1/2}\mathbf{M}_i\mathbf{Y}_i^{-1}(\mathbf{V}+\mathbf{A}_i\mathbf{H}_i\overline{\mathbf{P}}\mathbf{H}_i^T\mathbf{A}_i^T)\mathbf{Y}_i^{-1}\mathbf{M}_i^T\mathbf{R}^{1/2}\\
&\quad=\mathbf{R}^{1/2}\mathbf{M}_i\mathbf{Y}_i^{-1}\mathbf{M}_i^T\mathbf{R}^{1/2}
\end{aligned}
$$

where the last equation is obtained by definition of $\mathbf{Y}_i$ in (26). The above derivation shows that $\mathbf{R}^{1/2}\mathbf{M}_i\mathbf{Y}_i^{-1}\mathbf{M}_i^T\mathbf{R}^{1/2}$ is idempotent for $i=0,\ldots,h$.

Thus, the eigenvalues of the rank-deficient matrix $\mathbf{R}^{1/2}(\mathbf{M}_i\mathbf{Y}_i^{-1}\mathbf{M}_i^T)\mathbf{R}^{1/2}$ are ones and zeros, and the maximum eigenvalue $\lambda^2_{MAX,i}$ (and $\lambda^2_{MAX,0}$ for $i=0$) is equal to one. It follows that: $(\lambda_{MAX,i}+\lambda_{MAX,0})^2=4$.

REFERENCES

[1] Y. Bar-Shalom, and T. E. Fortmann, "Tracking and Data Association," *Mathematics in Science and Engineering*, Vol. 179, Academic Press, 1988.

[2] T. Bailey, "Mobile Robot Localisation and Mapping in Extensive Outdoor Environments," *PhD Dissertation*, The University of Sydney, 2002.

[3] T. Bailey and J. Nieto, "Scan-SLAM: Recursive Mapping and Localisation with Arbitrary-Shaped Landmarks," *Workshop at IEEE RSS 2008*, Zurich, Switzerland, 2008.

[4] A.J. Cooper, "A Comparison of Data Association Techniques for Simultaneous Localization and Mapping," *M.S. Thesis*, Massachussetts Institute of Technology, 2005.

[5] S. T. Pfister, K. L. Kriechbaum, S. I. Roumeliotis, J. W. Burdick, "Weighted Range Sensor Matching Algorithms for Mobile Robot Displacement Estimation," *Proc IEEE ICRA*, 2002.

[6] S.T. Pfister, S.I. Roumeliotis, J.W. Burdick, "Weighted Line Fitting Algorithms for Mobile Robot Map Building and Efficient Data Representation Robotics and Automation," *Proc. IEEE ICRA*, 2003.

[7] I. Tena Ruiz, Y. Petillot, D. M. Lane, and C. Salson, "Feature Extraction and Data Association for AUV Concurrent Mapping and Localisation," *Proc. IEEE-ICRA*, 2001.

[8] S. Thrun, "Robotic Mapping: A Survey," *Exploring Artificial Intelligence in the New Millenium*, G. Lakemeyer and B. Nebel, February 2002.

[9] S. Thrun, W. Burgard, and D. Fox, "A Probabilistic Approach to Concurrent Mapping and Localization for Mobile Robots," *Machine Learning and Autonomous Robots*, Vol. 31, No. 5, 1998, pp. 1-25.

[10] S. Thrun, W. Burgard, and D. Fox, "A Real-Time Algorithm forMobile Robot MappingWith Applications to Multi-Robot and 3D Mapping," *Proc. IEEE ICRA 2000*, San Francisco, CA, 2000.

[11] V. Nguyen, A. Martinelli, N. Tomatis, and R. Siegwart, "A Comparison of Line Extraction Algorithms using 2D Laser Rangefinder for Indoor Mobile Robotics," *Proc. IEEE/RSJ IROS*, 2005.

[12] Nunez, P.; Vazquez-Martin, R. del Toro, J.C. Bandera, A., "Feature Extraction from Laser Scan Data based on Curvature Estimation for Mobile Robotics," *Proc. IEEE ICRA*, 2006.

[13] Y. Li, E.B. Olson, "A general purpose feature extractor for light detection and ranging data," *Sensors*, Vol. 10, No. 11, 2010.

[14] R. Madhavan, H. Durrant-Whyte, and G. Dissanayake, "Natural Landmark-based Autonomous Navigation using Curvature Scale Space," *Proc. IEEE-ICRA*, 2002.

[15] D. Maksarov, and H. Durrant-Whyte, "Mobile Vehicle Navigation in Unknown environments: a multiple hypothesis approach," Proc. IEEE Control Theory Applications, Vol. 142 No. 4, 1995, pp. 385-400.

[16] E. Ackerman, "Google's Autonomous Cars Are Smarter Than Ever at 700,000 Miles," 2014.

[17] fars.NHTSA.dot.gov. Fatality analysis reporting system. Technical report, National Highway Traffic and Safety Administration, 2014.

[18] National Highway Traffic Safety Administration. National motor vehicle crash causation survey: Report to congress. Technical Report DOT HS 811 059, U.S. Department of Transportation, 2008.

[19] RTCA Special Committee 159, "Minimum Aviation System Performance Standards for the Local Area Augmentation System (LAAS)," *RTCA/DO-245*, 2004, Appendix D.

[20] Y.C. Lee, "Analysis of Range and Position Comparison Methods as a Means to Provide GPS Integrity in the User Receiver," *Proc. of the 42nd*

Annual Meeting of The Institute of Navigation, Seattle, WA, 1986, pp. 1-4.

[21] B.W. Parkinson, and P. Axelrad, "Autonomous GPS Integrity Monitoring Using the Pseudorange Residual," *NAVIGATION*, Vol. 35, No. 2, 1988, pp. 225-274.

[22] RTCA Special Committee 159, "Minimum Operational Performance Standards for Global Positioning System/Wide Area Augmentation System Airborne Equipment," RTCA/DO-229C, 2001, pp. 1-21.

[23] J. Leonard, and H. Durrant-Whyte, "Directed Sonar Sensing for Mobile Robot Navigation," *Kluwer Academic Publishers*, Cambridge, MA, 1992, pp. 129-138.

[24] S.B. Williams, G. Dissanayake, and H. Durrant-Whyte, "An efficient Approach to the Simultaneous Localisation and Mapping Problem," *Proc. IEEE-ICRA*, 2002.

[25] F. Lu and E. Milios, "Globally Consistent Range Scan Alignment for Environment Mapping," Autonomous Robots 4, 1997, pp. 333-349.

[26] T. Röfer, "Using Histogram Correlation to Create Consistent Laser Scan Maps," *Proc. IEEE IROS-2002*, Lausanne, Switzerland, 2002, pp. 625-630.

[27] A. Diosi and L. Kleeman, "Laser scan matching in polar coordinates with application to SLAM," *Proc. IEEE/RSJ IROS,* 2005.

[28] O. Bengtsson and A.J. Baerveldt, "Robot localization based on scan-matching-estimating the covariance matrix for the IDC algorithm," *Robotics and Autonomous Systems*, Vol. 44, 2003, pp. 29–40.

[29] M. Joerger, and B. Pervan, "Measurement-Level Integration of Carrier-Phase GPS and Laser-Scanner for Outdoor Ground Vehicle Navigation," *ASME Journal of Dynamic Systems, Measurement, and Control*, Vol. 131, 2009.

[30] Y. Bar-Shalom, F. Daum, and J. Huang, "The Probabilistic Data Association Filter," *IEEE Control Systems Magazine*, 2009, pp. 82-100.

[31] F.C. Chan, M. Joerger, S. Khanafseh, and B. Pervan, "Bayesian Fault-Tolerant Position Estimator and Integrity Risk Bound for GNSS Navigation," *Journal of Navigation of the RIN*, available on CJO2014, doi:10.1017/S0373463314000241, 2014.

[32] J. Areta, Y. Bar-Shalom, and R. Rothrock, "Misassociation Probability in M2TA and T2TA," *J. of Advances in Information Fusion*, Vol. 2, No. 2, 2007, pp. 113-127.

[33] B. DeCleene, "Defining Pseudorange Integrity – Overbounding," *Proc. of ION GPS 2000*, Salt Lake City, UT., 2000, pp. 1916-1924.

[34] J. Rife, S. Pullen, P. Enge, and Boris Pervan, "Paired Overbounding for Nonideal LAAS and WAAS Error Distributions." *IEEE TAES*, Vol. 42, No. 4, 2006 pp. 1386-1395.

[35] M. Joerger, "Carrier Phase GPS Augmentation Using Laser Scanners and Using Low Earth Orbiting Satellites," Ph.D. Dissertation, Illinois Institute of Technology,

[36] F. Bayoud, "Vision-Aided Inertial Navigation Using a Geomatics Approach," *Proc. ION GNSS*, Long Beach, CA, 2005.

[37] G. Dissanayake, P. Newman, S. Clark, H. Durrant-Whyte, and M. Csorba. "A Solution to the Simultaneous Localization and Map Building (SLAM) Problem." *IEEE Transactions on Robotics Automation*. 17.3 (2001): 229-241

[38] C. Ye, and J. Borenstein, "Characterization of a 2-D Laser Scanner for Mobile Robot Obstacle Negotiation," *Proc. IEEE-ICRA*, May 2002.